μSR and NMR: fundamental concepts and selected examples

Roberto De Renzi

Dipartimento di Fisica, Parma, Italy

1 Introduction

Nuclear magnetic resonance (NMR) and μSR represent two ways of performing essentially the same experiment. They employ, of course, different probes—respectively the nuclei, which are natural components of the sample, and the muon, an implanted guest. The detection technique is also different and the consequences of their peculiarities are large. They fully justify, for instance, the omni-presence of NMR spectrometers in chemistry departments (or in hospitals) where muons are scarcely frequented, while in magnetism the balance of the two techniques is perhaps reversed. However NMR and μSR are conceptually the same and exploiting the analogy should help understanding both of them.

No serious attempt at a systematic comparison between the two is within the scope of these lectures: any scientific library provides already numerous large books on the basics of each of them. For the sake of a pedagogical introduction I shall instead focus on a small number of examples, chosen to illustrate the close nature of NMR and μSR, allowing at the same time a few of their distinct merits to emerge.

Section 2 consists of a very crude description of the basic NMR experiments, compared to their muon equivalent. It leads onto a re-discussion of a few fundamental concepts, like longitudinal and transverse relaxation, in a language slightly different from that most familiar to the muon community. All that is written here can be found in many standard textbooks. They will not be quoted extensively; it suffices perhaps to do it now by saying that some texts (Abragam 1961, Slichter 1990) are basic and thorough, some (Fukushima and Röder 1981) are very introductory and hardware oriented, while some (Abragam and Goldman 1982, Ernst *et al.* 1987) are more advanced.

The remaining sections of this chapter are devoted to two topics where NMR and μSR have both contributed. Section 3 is focused on relaxation in metals and superconductors, with one example of historic relevance and some more recent ones. Section 4 considers critical fluctuations in simple antiferromagnets, the classic example where NMR first proved its merits when opening up the field and μSR later added renewed insight.

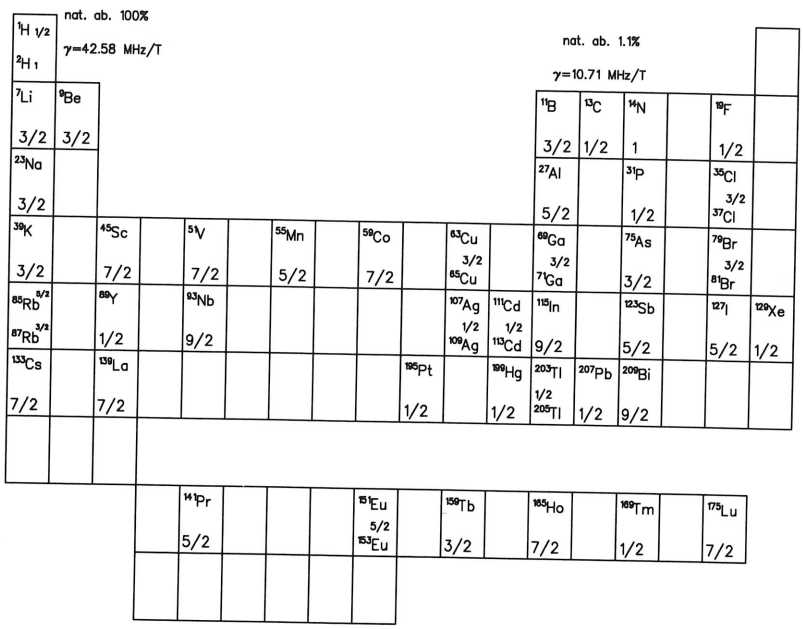

Figure 1. *A periodic table of the NMR most used nuclei*

2 The basic NMR experiment compared to μSR.

Both NMR and μSR consist in the measurement of the time evolution of the magnetic moment of a probe. The muon magnetic moment has already been introduced. As for the nucleus virtually all chemical elements have at least one isotope which possesses a non zero spin, *i.e.* a magnetic moment. However in quite a few instances the suitable ones are rare in natural compounds. Figure 1 shows a periodic table with some of the most useful nuclear species, say, the first choices of an NMR user. Two parameters guide this rather arbitrary selection: the natural abundance of the isotopes with non zero spin (the only two rare isotopes included are ^{2}H and ^{13}C, for their wide NMR use in chemistry) and a reasonably large nuclear magnetic moment, quantified by the gyromagnetic ratio γ.

Only a few of the isotopes appearing in this table have spin $I = 1/2$. For isotopes with $I > 1/2$ nuclear magnetic resonance has to cope also with the electric quadrupole moment of the nucleus (which, by Wigner-Eckart theorem, is associated with non zero angular momentum). The quadrupole moment q couples to electric field gradient $\underline{\mathbf{V}}$ by

$$\mathcal{H} = \frac{eq\hbar}{4I(2I-1)}\mathbf{I}\cdot\underline{\mathbf{V}}\cdot\mathbf{I} \tag{1}$$

where $\underline{\mathbf{V}}$ is a tensor which may be due to ionic charges, whenever the lattice has at least a partial ionic character, but it has also electron contributions from the on-site shells. It is worth mentioning that this interaction may produce level splittings well within the radio frequency (RF) range, and the direct excitation of their transitions, in the absence of an external magnetic field, is called Nuclear Quadrupole Resonance (NQR). We shall

not describe NQR and the structural information it can provide, as this may well be the topic for a separate series of lectures.

In both NMR and μSR the magnetic moment is monitored as an ensemble average over a large number of individual probes, hence a net spin polarisation, or magnetisation is required to start with. While all muon beams rely on parity violation in the pion decay to provide nearly 100% polarisation, the nuclear magnetisation, $\mathbf{M}$, can only be built complying with thermodynamic equilibrium. Perhaps the most common case is with a magnetic field applied to the sample, resulting in a Zeeman splitting of the nuclear spin levels, and in

$$\mathbf{M} = \chi \mathbf{H} = \frac{N\mu^2}{3k_B T}\mathbf{H}, \tag{2}$$

by Curie law. This law corresponds to a first order approximation of the difference between the Boltzmann population of the Zeeman energy levels. Incidentally, following the same approach a similar magnetisation, inversely proportional to temperature, is obtained in the NQR case. Therefore the nuclear signal intensity is always temperature dependent: in the absence of other effects, it is much stronger at low temperature. Equation 2 also shows that in NMR proper (not in NQR) a large external field is *needed*, to start with.

In order to stress the nucleus-muon analogy it is easier to refer to *pulse* NMR, which nowadays dominates over older *continuous wave* schemes. Pulse sequences may be extremely complex and we shall describe only the three most simple ones. Their starting step consists in selecting different initial spin states. The selection, which is achieved also in μSR by simply choosing a spectrometer geometry (the spin polarisation being given), is reached in NMR by tuning the RF resonant pulse duration. Transverse field (TF) μSR corresponds to a one pulse, $\pi/2$, NMR experiment, while Longitudinal field (LF) μSR may be compared to slightly more complex pulse sequences, based on the π pulse. In order to show how they work and to justify their names we shall recall a few elementary concepts which follow from Larmor theorem.

2.1 Classical treatment of the spin precession

In the laboratory frame the classical time evolution of an angular momentum $\mathbf{I}$ is expressed in terms of the torque, $\gamma\hbar\mathbf{I}\times\mathbf{B}$ in the presence of an external field $\mathbf{B}$. For the macroscopic nuclear magnetisation $\mathbf{M}$, *i.e.* the sum of magnetic moments $\gamma\hbar\mathbf{I}$ over a unit volume, the following well known equation is obtained

$$\frac{d\mathbf{M}}{dt} = \gamma\mathbf{M}\times\mathbf{B}. \tag{3}$$

This type of equation determines the Larmor precession. The standard way to view it is to move onto a rotating reference frame (RRF). Let us choose $\mathbf{B} = B\hat{\mathbf{z}}$ and the frame revolving with angular velocity $\mathbf{\Omega} = \Omega\hat{\mathbf{z}}$, such that its axes are $\{\hat{\mathbf{x}}', \hat{\mathbf{y}}', \hat{\mathbf{z}}\}$. In the RRF there is an apparent torque and the equation of motion reads

$$\frac{\partial\mathbf{M}}{\partial t} = \gamma\mathbf{M}\times\mathbf{B} + \mathbf{M}\times\mathbf{\Omega}.$$

Thus $\mathbf{M}$ experiences an *effective* field $\mathbf{B}_{\text{eff}} = (B+\Omega/\gamma)\hat{\mathbf{z}}$. If $\Omega = -\gamma B$, hence $\partial\mathbf{M}/\partial t = 0$, the equation tells us that $\mathbf{M}$ is stationary in the RRF: this is the Larmor precession. But the concept of an effective field in also precious in other RRF as we shall presently see.

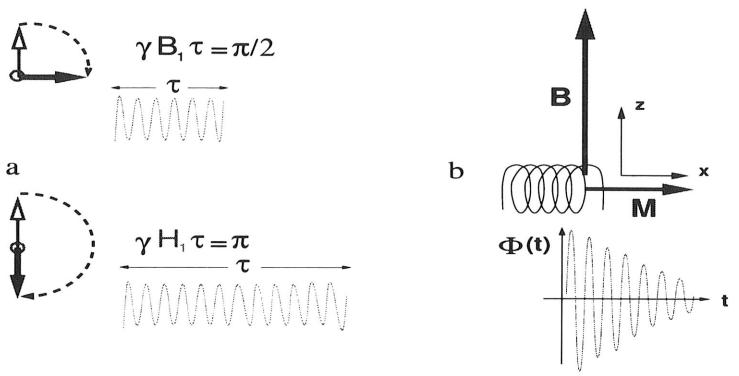

Figure 2. *(a) Relation between* RF *field intensity* B_1*, pulse duration* τ *and nutation angle; (b) FID detection: if at* $t = 0$ $\mathbf{M}$ *lies along* $\hat{\mathbf{x}}$ *the coil is subject to an e.m.f.* $\Phi(t)$*).*

If now we apply also a rotating field $\mathbf{B}_1(t) = B_1\,[\hat{\mathbf{x}}\cos\omega t + \hat{\mathbf{y}}\sin\omega t]$ we may chose the RRF where $\mathbf{B}_1$ appears static, i.e $\Omega = \omega$. In this reference frame there is an effective field

$$\mathbf{B}_{\text{eff}} = \left(B + \frac{\omega}{\gamma}\right)\hat{\mathbf{z}} + B_1\hat{\mathbf{x}}'.$$

By tuning the RF frequency to the Larmor condition $\omega = \omega_L = -\gamma B$, the effective field component along $\hat{\mathbf{z}}$ vanishes and we are left with a "static" field $B_1\hat{\mathbf{x}}'$ in the RRF. As long as the RF field is on the magnetisation precesses around it, rotating through angles fixed by the duration τ of the RF pulse, $\phi = \gamma B_1 \tau$ (see Figure 2a and b). In the laboratory frame the motion is actually a *nutation.*

The motivation for rehearsing these simple arguments is to underline the intrinsic *resonant* nature of this process, which is indeed relevant for all time dependent local fields, and for muons as well, not only for the coherent RF excitation of NMR. The resonance comes into play twice: first one trivially needs a resonant circuit to drive a RF current through a coil and produce $B_1(t)$, but, second, more subtly, the effective field produces a nutation as long as it is nearly perpendicular to the initial direction of $\mathbf{M}$, *i.e.* $\hat{\mathbf{z}}$. Note that If the RF pulse duration corresponds to $\pi/2$ nutation at resonance, *i.e.* for $\omega = -\gamma B$, the transverse spin component for nuclei probing different static fields ($\omega = -\gamma B'$) is really $\sin\theta\sqrt{1-\cos\phi}$, approximated in the figure by $\sin\theta$.

Thus a rough measure of the transverse component of the transverse magnetisation is given by the sine of the angle θ between $\mathbf{B}_{\text{eff}}$ and $\mathbf{B}$, which turns out to be

$$\sin\theta = \frac{B_1}{\gamma\sqrt{(B+\omega/\gamma)^2 + B_1^2}}$$

and it is shown in Figure 3 as a function of frequency, for $B_1 \ll B$. This is clearly a resonant process, whose frequency breadth depends on the relative strength of the two Zeeman interactions (that with the static and that with the time dependent field).

The core of an NMR spectrometer is therefore a coil in a tuned circuit, *e.g.* a small solenoid, which is selectively coupled to a transmitter, for high power input, and to a

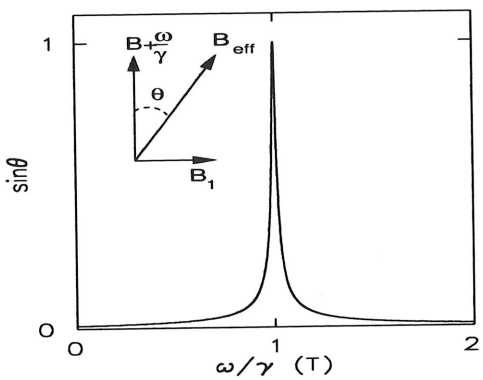

Figure 3. *Effective field and its transverse component ($\propto \sin\theta$) in the RRF as a function of frequency.*

receiver, for low level signals. The field generated by the transmitter RF pulse is $B_1\hat{\mathbf{x}}\cos\omega t$, which is the sum of a rotating field, with $\mathbf{\Omega}=\omega\hat{\mathbf{z}}$, and a counter rotating field ($-\omega\hat{\mathbf{z}}$). The second is totally negligible, being out of resonance. The receiver then measures an e.m.f. due to the precession of $\mathbf{M}$ around $\mathbf{B}$ inside the coil (Figure 2b). Since the precession signal decays, while the initial amplitude of the coherent magnetisation is progressively lost, the nuclear precession signal is called Free Induction Decay (FID).

2.2 Bloch equations

The examples illustrated in Sections 3.1 and 4 deal with longitudinal and transverse relaxation, a topic which is already discussed in many other lectures of this school. Still it is perhaps useful to follow here the typical NMR approach to the concept of relaxation.

Imagine we just switched off the RF pulses, which have conveniently driven the initial magnetisation out of thermodynamic equilibrium. The simplest description of its time evolution is given by a set of well known phenomenological equations, first proposed back in 1946 by Felix Bloch

$$\begin{aligned} \frac{dM_x}{dt} &= \gamma B M_y - \frac{M_x}{T_2} \\ \frac{dM_y}{dt} &= -\gamma B M_x - \frac{M_y}{T_2} \\ \frac{dM_z}{dt} &= -\frac{M_z - \chi B}{T_1}. \end{aligned} \tag{4}$$

They correspond to Equation 3, with the addition of two separate *rate equation* terms: $(M_z - M_{0z})/T_1$, which represents an exponential recovery of the equilibrium value $M_{0}z = \chi B$, and $M_{x,y}/T_2$ which represent the effects of spin interactions (or static field inhomogeneity) on the transverse components of $\mathbf{M}$. This second term does not involve a change in the Zeeman energy of the spin system, therefore it does not directly lead the system back towards thermodynamic equilibrium.

It is worth stressing that T_1^{-1} relaxation is vital for NMR. If it were not for this relaxation, one could never build up the nuclear magnetisation along the static magnetic field (Equation 2) in a sample. This process must be very carefully considered also when repeating experiments (*e.g.* for noise reduction by averaging): pulse NMR detection requires an out of equilibrium **M**, but in general the equilibrium must be restored before the next sequence starts.

In Bloch equations the exponential behaviour for both longitudinal and transverse components of the magnetisation (M_z and $M_+ = M_x + iM_y$) is merely assumed. This is *not* the general case, for a variety of reasons, although the condition is luckily fulfilled in many interesting instances. We shall discuss the approximations in Section 2.4.

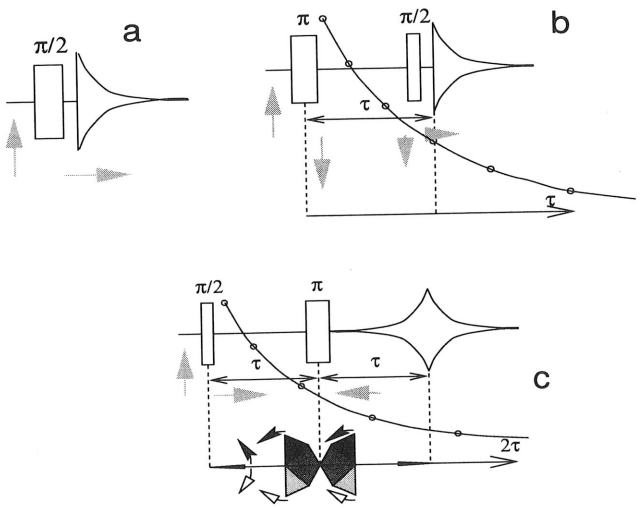

Figure 4. *Three basic NMR pulse sequences. The horizontal axis corresponds to time, the rectangular box to a* RF *pulse and the exponential envelope to the signal detection. The arrow indicates the magnetisation direction in the* $(\hat{\mathbf{z}}, \hat{\mathbf{x}}')$ *plane at different instants. a) One* $(\pi/2)$ *pulse; b) Inversion recovery; c) Spin echo. In b) and c) the time dependence of the detected signal amplitude is overlayed.*

2.3 Elementary pulse sequences

Let us first see how the two relaxation rates, T_1^{-1} and T_2^{-1}, may be directly measured in NMR. Figure 4 illustrates three basic pulse sequences. Panel (*a*) illustrates the single pulse, yielding a $\pi/2$ nutation of **M** and the subsequent observation of a FID. The convention is to imagine a horizontal time axis: the rectangular box represents the RF pulse, immediately followed by signal acquisition (the double exponential envelope). The sketch shows a time delay between the pulse and the FID, which emphasises the inherent dead time of electronic detection - the nuclear signal really starts as soon as a transverse magnetisation appears. The black arrows indicate the direction of **M** in the RRF, at a point in time corresponding to the arrow base: in the $\pi/2$ pulse case, immediately after the pulse, **M** is turned by 90 degrees into the precession plane.

The decay rate of the FID itself is a measure of T_2^{-1}. Following the NMR convention this rate, which is actually the line width of the NMR spectrum, is called T_2^{*-1}, to stress the fact that all sources of dephasing in the precession contribute to it, including the trivial field inhomogeneity of the magnet. Less trivial ones come from inhomogeneous distributions of local interactions (only the secular components contribute, i.e those commuting with the Zeeman Hamiltonian). The T_2^{*-1} is the exact analogue of the TF μSR line width.

Figure 4*b* shows the so-called *inversion recovery*, one of the sequences which yield the longitudinal rate T_1^{-1} (equivalent to a LF μSR experiment). By the same conventions it is composed of a π pulse, which reverts $\mathbf{M}$, a waiting time τ during which $\mathbf{M}$ relaxes towards equilibrium, and a detection $\pi/2$ pulse, which brings the residual $\mathbf{M}(\tau)$ in the precession plane, to yield the FID. The initial FID amplitude decays as $\exp(-\tau/T_1)$.

Finally a very important sequence is the Hahn echo, depicted in Figure 4*c*. The first pulse turns $\mathbf{M}$ by 90 degrees. The static inhomogeneity of the local field spreads out M_+, as seen in the RRF, like the fan shown at the bottom of the panel: some spins precess faster and others slower than the average. The curved arrows indicate the direction of their precession in the RRF. The second pulse, after a time delay τ, turns all spins by π around $\hat{\mathbf{y}}'$, *i.e.* it reverts their precession phase. It is easy to see that the same differences in Larmor frequencies which caused the opening of the fan, will now close it, and exactly after a time τ. This produces the echo signal in the coil.

The amplitude of the echo is not affected by the inhomogeneity of the external field. Since also a distribution of local fields from secular interactions is refocused by the π pulse, the signal amplitude as a function of 2τ measures all contributions to the line width parameter, T_2^*, *but* these static inhomogeneities. The rate measured by spin echoes is referred to as T_2^{-1}, proper. It may be measured also in μSR, but only by employing similar coherent RF pulse techniques, which have been demonstrated, for instance at ISIS. In practice, while the spin echo is an every-day tool in NMR, it is still just demonstrative for muons.

2.4 Relaxation: the interactions

What is the cause of the T_1 relaxation? In order to have a modification of the population of different energy levels we must induce transitions among them. The only way to do this is by a time dependent perturbation. The RF field was one such case, but coupling to other degrees of freedom of the system (generically referred to as the lattice) may be also seen as a time dependent perturbation.

Let us consider a generic coupling to the lattice as a time dependent perturbation. It is convenient to write its Hamiltonian term as

$$\mathcal{H}_1(t) = \sum_l F_l(t) A_l \tag{5}$$

separating the time-dependent coupling constants, F_l, and the spin operators, A_l. This is a very general expression, but in many instances the interaction acts simply as a local fluctuating field $\mathbf{B}_l$, like in the case of a hyperfine coupling to a fluctuating electron spin

$$\mathcal{H}_1(t) = \hbar\omega_0 \mathbf{I} \cdot \mathbf{S}(t) = \gamma\hbar \mathbf{I} \cdot \mathbf{B}_l(t).$$

A specific NMR example of a coupling with the lattice which cannot be written as a local magnetic field is phonon modulation of a quadrupolar interactions. Recalling Equation 1, one may have a time dependent electric field gradient, modulated by phonons. This is a tensor, not a vector field, and the interaction is bilinear in the spin operator $\mathbf{I}$. Since all interactions between the lattice and the muon, thanks to its spin 1/2, can always be written in terms of a local magnetic field we shall restrict ourselves to this simpler case.

We want to show a semi classical derivation of relaxation rates: we wish to treat the probe spin according to quantum mechanics and the lattice excitations as a classical random process. Let us consider again Bloch equations (4), which are of the form

$$\frac{dM_\alpha}{dt} = -kM_\alpha \qquad (\alpha = x, y, z).$$

The nuclear magnetisation - we shall refer to this quantity for the sake of simplicity but the same treatment could be performed for the muon spin polarisation - is given by a double average, $M_\alpha \propto \langle \overline{I_\alpha} \rangle$. Here $\overline{A}$ means the average of the observable A over the random variables and $\langle A \rangle = \mathrm{Tr}\,(\sigma A)$ the average over the probe spin states, written explicitly in terms of the density matrix σ.

Since the time evolution of σ is governed by the Schrödinger equation

$$\frac{d\sigma}{dt} = -\frac{i}{\hbar}\left[\mathcal{H}_0 + \mathcal{H}_1(t), \sigma\right] \tag{6}$$

and the other time dependence, namely that of the lattice excitations, is treated as a random process, one has

$$\frac{dM_\alpha}{dt} \propto \mathrm{Tr}\, I_\alpha \overline{\frac{d\sigma}{dt}}. \tag{7}$$

This equation is the same as the Bloch equation, *i.e.* it yields a rate k, provided

$$\mathrm{Tr}\, I_\alpha \overline{\frac{d\sigma}{dt}} = -k\, \mathrm{Tr}\, \overline{(\sigma I_\alpha)} \tag{8}$$

which is then a rigorous condition for an exponential relaxation to take place. Before proceeding to derive a general expression for the relaxation rates it is worth pointing out that non-single-exponential relaxations routinely take place in NMR for spin $I > 1/2$ species. In this case the Zeeman levels of each spin are more than two and it is convenient to write the M_α in terms of the level populations. Equation 7 then becomes a matrix equation with as many solutions as the allowed transitions, hence the relaxation is a linear combination of exponentials (Andrew and Tunstall 1961, Ernst *et al.* 1987).

Coming back to the simple $I = 1/2$ case we must work out the left hand side of Equation 8. We already know what spin dynamics to expect: it will be a damped precession and we can get rid of the trivial harmonic motion by moving to the RRF. In quantum mechanics the equivalent of this is (broadly speaking) the unitary transformation to the interaction representation, given by:

$$\begin{aligned} \sigma^I(t) &= e^{i\mathcal{H}_0 t/\hbar}\sigma e^{-i\mathcal{H}_0 t\hbar} \\ \mathcal{H}_1^I &= e^{i\mathcal{H}_0 t}\mathcal{H}_1 e^{-i\mathcal{H}_0 t} \\ \mathcal{H}_0 &= -\hbar\omega_L I_z. \end{aligned}$$

The Schrödinger Equation (6) may be rewritten, up to second order in $\mathcal{H}_1$ as

$$\frac{d\sigma^I}{dt} = -\frac{1}{\hbar^2}\int_0^\infty d\tau \overline{[\mathcal{H}_1^I(t), [\mathcal{H}_1^I(t-\tau), \sigma^I(t)]]} \tag{9}$$

which is just the Fermi golden rule.

We can now spell out the interaction (for the details see the appendix)

$$\mathcal{H}_1^I(t) = \gamma\hbar\left[B_{ez}(t)I_z + \frac{1}{2}\left(B_{e+}(t)I_+e^{-i\omega_L t} + B_{e-}(t)I_-e^{i\omega_L t}\right)\right]$$

where we have written explicitly the components of the local fluctuating field (in particular $B_{l\pm} = B_{lx} \pm iB_{ly}$ are those orthogonal to $\mathbf{B}$). If we introduce this expression in the Fermi golden rule, put it back in the left hand side of Equation 8 and sort out the commutators, we recover the exponential decay of Bloch equations. For instance considering the z component of $\mathbf{M}$ we get

$$\frac{d\overline{\langle I_z\rangle}}{dt} = -\left[\gamma^2\int_0^\infty d\tau e^{i\omega_L\tau}\overline{B_{l+}(\tau)B_{l-}(0)}\right]\overline{\langle I_z\rangle} \tag{10}$$

and the expression in square brackets is the rate T_1^{-1}

Since this is the very foundation of a quantity directly accessible to experimental determination, it is worthwhile to include a completely worked out example. The appendix shows the derivation of the rates for one of the simplest cases, that of an isotropic hyperfine coupling in an isotropic medium.

By Equation 10 it follows that the longitudinal relaxation rate is proportional to the Fourier transform of the local field correlation function, evaluated at the Larmor frequency ω_L. In the simple case of the appendix the field correlation function coincides with the electron spin autocorrelation function, *i.e.* the response function of the electron system. In general - we shall see one such instance in Section 4 the relation between relaxation rates and electron response function is less direct. The Fourier transforms, $J(\omega)$ of correlation functions are often referred to as *spectral densities.*

Note that, since the spin precession is an intrinsically resonant phenomenon, as it was pointed out in Section 2.1 and in Figure 3, its relaxation resonantly picks up only one component of the possibly much wider spectrum $J(\omega)$ of the fluctuating local fields.

We can now derive a very useful basic approximation, which was already introduced in other lectures by intuitive arguments. The area under $J(\omega)$ is the Fourier anti transform at $t = 0$

$$\int_{-\infty}^{\infty} d\omega J(\omega) = \left(\overline{B_l(0)B_l(0)}\right) = B_l^2,$$

the square of the instantaneous local field. Beware that this quantity depends strongly on the structure of the nuclear neighbourhood. It may be different before and after solidification of a fluid; it is clearly very different in a paramagnet and in an antiferromagnet. As long as the square mean field is constant with temperature, we can approximate the area under $J(\omega)$ as a height, $J(0)$, times the width τ^{-1} (the inverse of a correlation time) and, if we further restrict ourselves to fast dynamics,

$$\tau \ll \omega_L,$$

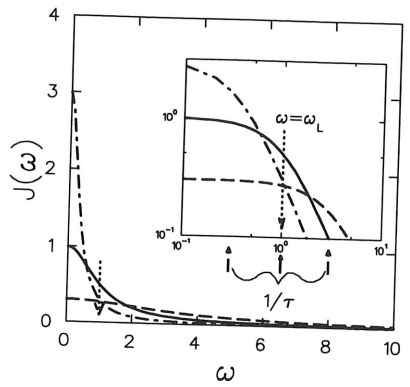

Figure 5. *Spectral density at* $T_1 < T_2 < T_3$.

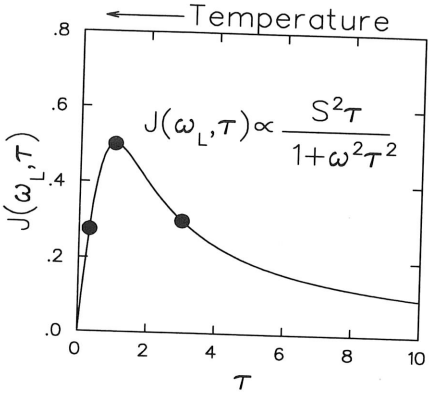

Figure 6. *Temperature dependence of the longitudinal relaxation rate*

we obtain $J(\omega_L) \approx J(0) = \gamma^2 B_l^2 \tau$. This means directly, for instance

$$T_1^{-1} = (\gamma B_l)^2 \tau, \tag{11}$$

which is the fast dynamics approximation for longitudinal relaxation rates.

Figure 5 illustrates a generic temperature dependent dynamics, represented by a Lorentzian

$$J(\omega) = \frac{\gamma^2 B_l^2 \tau}{1 + \omega^2 \tau^2},$$

with *e.g.* an activated correlation time $\tau = \tau_0 \exp(-T_a/T)$. Since $J(\omega)$ becomes broader with increasing temperature, but it conserves its area, meanwhile the longitudinal relaxation rate (Figure 6) develops a peak: its maximum corresponds to the condition $\omega_L = \tau^{-1}$. The transverse relaxation, resulting from

$$\frac{d\overline{\langle I_+ \rangle}}{dt} = -\left[\gamma^2 \left(\int_0^\infty d\tau \overline{B_{lz}(\tau) B_{lz}(0)} + \frac{1}{2} \int_0^\infty d\tau e^{i\omega_L \tau} \overline{B_{l-}(\tau) B_{l+}(0)} \right) \right] \overline{\langle I_+ \rangle} \tag{12}$$

has a different behaviour in the static limit. It has an additional contribution proportional to $J(0)$ (see Appendix), corresponding to the static line width, and when the dynamic contribution freezes out at low temperature ($\tau > \omega_L^{-1}$), T_2^{-1} reaches a constant value.

3 Relaxation in metals and semiconductors

We start by considering the effect of the spin interaction with electrons in simple metals, treated as a free electron gas. This is an introductory example and the basis for understanding more complex cases, like the superconducting state and the subtle effects of electronic correlation.

From an experimental point of view NMR of good metals is not at all straightforward, since the skin depth at radio frequencies, the distance over which electromagnetic fields are screened, may be as short as few hundreds nm. Fine powders are often employed and single crystal studies may be out of question. μSR has no such restrictions, of course.

3.1 Korringa relations

The precession spectrum of both muons and nuclei displays the Knight shift, which is extensively discussed in Alex Schenck's lectures in this volume.

In few words its represents a local field contribution due to the electron gas polarised by the external field. The small polarisation is given by the temperature independent Pauli susceptibility $\chi_P = (1/2)\gamma_e^2\hbar^2 g(E_F)$, proportional to the density of state g at the Fermi energy.

Recall that the Knight shift constant, defined in terms of the experimental precession frequency ν and the Larmor frequency ν_L as $(\nu - \nu_L)/\nu_L$, is

$$K = \frac{8\pi}{3}\langle|\psi_k(r=0)|^2\rangle_F \chi_P. \tag{13}$$

Here $\langle\rangle_F$ indicates the average over the Fermi surface and $(8\pi/3)\,|\psi_k(0)|^2$ is the contact hyperfine coupling with electrons of wave vector $\mathbf{k}$, which carry a magnetic moment given by Pauli susceptibility

$$\hbar\gamma\langle S\rangle = \chi_P \mu_0 H.$$

We are concerned here by the relaxation effects due to the same local field

$$\mathbf{B}_e(\mathbf{k},t) = \frac{8\pi}{3}\hbar\gamma_e\,|\psi_{\mathbf{k}}(0)|^2\,\mathbf{S}(\mathbf{k},t),$$

bearing in mind that the small Knight shift is the combined effect of a large instantaneous value of B_e and of a very fast dynamics.

In order to obtain the relaxation rate we could employ the formalism of Section 2.4, that is we could consider the field self correlation function and average it over the band. It is simpler to justify directly an intermediate step of the calculation, originally due to Korringa

$$\frac{1}{T_1} = \frac{2\pi}{\hbar}\frac{1}{2}\left(\frac{8\pi}{3}\hbar\gamma_e\hbar\gamma\langle|\psi_{\mathbf{k}}(0)|^2\rangle_F\right)^2 \int g^2(E)\,f(E)(1-f(E))\,dE \tag{14}$$

$$= \frac{64\pi^3}{9}\hbar^3\gamma_e^2\gamma^2\,\langle|\psi_{\mathbf{k}}(0)|^2\rangle_F^2\,g^2(E_F)\,k_B T. \tag{15}$$

The first line corresponds to the transition probability, by Fermi golden rule), induced by the hyperfine coupling between electron states of equal energy. The energy conservation condition follows from the fact that nuclear energies are negligible ($\hbar\omega_L \ll E_F$). The electron interaction drives a nuclear spin transition, whose square matrix element gives the further factor 1/2. The square of the density of states times the two factors containing the Fermi-Dirac distribution f represent the probability of finding an *occupied initial* electron state and an *final unoccupied* state.

The same result, within a small numeric factor, may be obtained by a back-of-the-envelope calculation. Since $\omega_e \simeq E_F/\hbar$ is much larger than ω_L we can estimate the rate for the free electron gas by Equation 11, considering that of all electrons in the band only a fraction $k_B T/E_F$ around the Fermi surface contributes to scattering. Then the rate is proportional to the fraction itself, to $\gamma^2 B_e^2(0)$ and to the correlation time, which may be estimated as $\hbar/E_F$. One can recognise all these factors in Equation 14, recalling that $g(E_F) = 1/E_F$ for the electron gas.

From the relaxation rate and Knight shift, Equations 13 and 15, we obtain the so-called *Korringa relation*

$$\frac{1}{T_1 T} = K^2 \frac{4\pi k_B}{\hbar} \left(\frac{\gamma}{\gamma_e}\right)^2, \tag{16}$$

which shows the following important point. The derivation of the Knight shift and of Korringa relaxation may be extended from the Fermi gas to the Fermi liquid case, with essentially the same results. Each of them depends on the hyperfine coupling and on the $g(E_F)$ of the real metal, the latter being very different from the simple Fermi gas expression. However their combination $T_1 T K^2$ is a universal constant. Thus combined measurements of the Knight shift and of the relaxation may evidence deviations from the strict Fermi liquid behaviour, which are a consequence of electron correlation.

To conclude this introductory topic let us evaluate the Korringa rates at room temperature for a typical metal, with a Knight shift constant of 10^{-4}. For a ^{63}Cu nucleus ($^{63}\gamma/\gamma_e \approx 4 \times 10^{-4}$) we get $T_1^{-1} = 1\ \mathrm{s}^{-1}$ which is well within the measurable range for NMR. However for muons ($\gamma_\mu/\gamma_e \approx 5 \times 10^{-3}$) we obtain $T_1^{-1} = 100\ \mathrm{s}^{-1}$, which corresponds to a decay time for the longitudinal polarisation of 4500 muon lifetimes, *i.e.* way too short to be measured. In the following section we shall encounter a peculiar muonium example where the Korringa rate could be measured. A subsequent recent NMR example gives a hint of further important aspects which may be tackled by this kind of experiments.

3.2 Relaxation in the superconducting state

For a normal metal the quantity $1/T_1 T$ is constant with temperature. Two features characterise the temperature dependence of the same quantity in the superconducting state: it rapidly goes to zero for $T \to 0$, and it is enhanced (it develops the so-called Hebel-Slichter peak) *just below* T_c.

The peculiar aspects of nuclear relaxation in the superconducting state were considered one of the first direct experimental evidences of the validity of the BCS theory. In short, nuclear relaxation is one experimental determination of the electron response function, *i.e.* of a process of scattering with electrons. Many others exist, including for instance ultrasonic attenuation. For normal electrons in the metallic state the two kind of response are just proportional to each other. For paired electrons in the superconducting state it is not so. The experimental demonstration and the detailed understanding of this point brought conclusive support for BCS.

The original work (Hebel and Slichter 1959) is worth reading directly for its clear exposition. We present their main result,

$$\frac{1}{T_1} \propto \int g_s^2(E,T)\, f(E)(1 - f(E))C(E,T)\, dE, \tag{17}$$

where

$$g_s(E,T) = g(E) \frac{E - E_F}{\sqrt{(E - E_F)^2 - \Delta(T)^2}}$$

is the BCS density of states, Δ the energy gap and

$$C(E,T) = \left(1 + \frac{\Delta(T)}{E - E_F}\right)$$

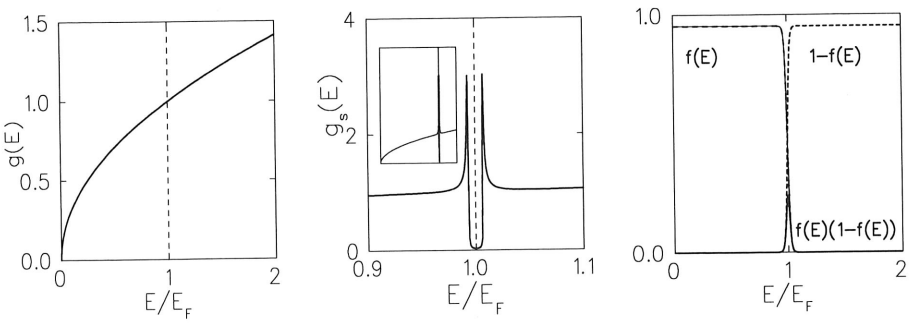

Figure 7. *a (left) - Normal density of states for the Fermi gas. b (center) - BCS density of states around E_F (the inset shows the full curve). c (right)- Fermi-Dirac functions product $f(E)(1-f(E))$ (solid line) and its factors (dashed lines)*

a coherence factor. Let us discuss these quantities in comparison with Equation 14, which represents the analogous derivation for the normal metallic state. The same integral appears in both expression, but the density of state changes and the BCS expression has an extra factor, C. We shall now describe the origin of this factor, its relevance, and its effect on the measured relaxation rates. To do this we need to discuss first the modifications of the density of states.

For the sake of simplicity we shall assume the Fermi gas features for the normal metal. Figure 7 shows a few of the ingredients of Equations 14 and 17. BCS theory is based on the formation of Cooper pairs, which are two electron states, the first of wave vector $\mathbf{k}$ and spin up ($\uparrow$), the second of wave vector $-\mathbf{k}$ and spin down ($\downarrow$). So one can try to describe the nuclear relaxation rate in terms of well defined single particle quantities (such as $g_s(E,T)$). It turns out that this is partially possible, and the probability of occupancy is still given by the Fermi-Dirac distribution, but the extra coherence factor C appears.

The shape of g_s is identical to that of g but for the gap region around the Fermi energy (detail shown in Figure 7b): single electron states are pushed out of the gap and pile up in a Van Hove singularity at its edges. This plot must be rescaled at each temperature below T_c, according to the BCS temperature dependence of the gap, shown in Figure 8.

A comparison of the two factors $g_s(E,T)$ and $f(E,T)(1-f(E,T))$, (Figure 7b,c) explains the first feature of $1/T_{1s}$: as the temperature is reduced, the peak of the Fermi-Dirac functions product narrows around E_F, while the gap in g_s broadens. This results in an exponential reduction of $1/T_{1s} \propto \exp(-k_B T/\Delta)$, which follows the exponential disappearance of the single electron excitations responsible for the scattering.

Also ultrasonic attenuation drops in a similar way below T_c. However, contrary to nuclear relaxation, it does not display the peak which we described at the beginning. The coherence factor $C(E,T)$, which peaks at the gap edges (hence its temperature dependence), is plotted in Figure 9. It represents an interference effect, the only part of the BCS description which cannot be reconciled with a single particle interpretation. It originates from the fact that Cooper pairs in the superconducting ground state (and in the thermally excited states orthogonal to it) are coherent linear superposition of two electron states:

$$u_k \left|\mathbf{k}\uparrow\right\rangle \left|-\mathbf{k}\downarrow\right\rangle + v_k \left|-\mathbf{k}\uparrow\right\rangle \left|\mathbf{k}\downarrow\right\rangle .$$

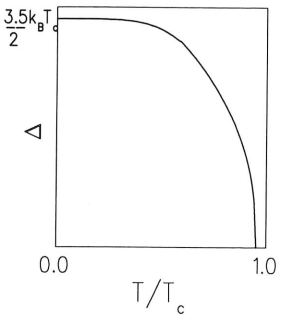

Figure 8. *Temperature dependence of the BCS gap $\Delta(T)$*

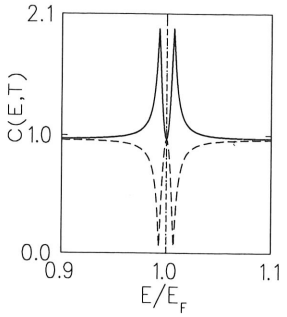

Figure 9. *The coherence factor $C(E,T)$: the solid curve is coherence for NMR relaxation, the dashed curve is for ultrasound scattering.*

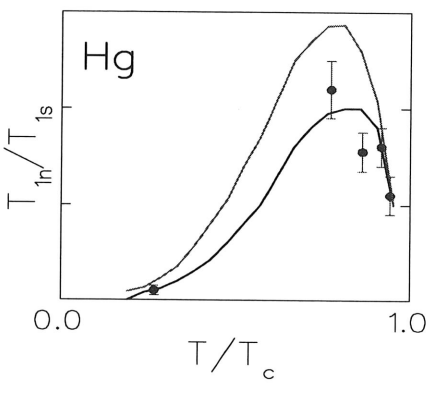

Figure 10. *The Hebel Slichter peak: Hg NMR relaxation rates, divided by temperature. The curves are the BCS theory (see text)*

Computing transition probabilities with such composite states rather than with simple ones ($|\mathbf{k}\uparrow\rangle\,|-\mathbf{k}\downarrow\rangle$) gives rise to interference terms, as in ordinary optics and wave mechanics, which peak at the edges of the gap.

Close enough to T_c the interference peaks in Figure 9 are within the k_BT width of the Fermi Dirac product of Figure 7c, hence the nuclear relaxation rate is larger that the corresponding normal state value. This is precisely the Hebel-Slichter peak in $1/T_1$, while a phase change in the coherence (dashed curve in Figure 9) yields an anti-peak in ultrasound attenuation.

Figure 10 shows a re elaboration of the original NMR data on Hg (Reif 1956), together with the BCS curves (Hebel and Slichter 1959). The two curves represent two values of a finite electron lifetime, which is the only adjustable parameter in the model. Notice that the data are plotted as $1/T_1T$, hence the normal behaviour is a straight horizontal line.

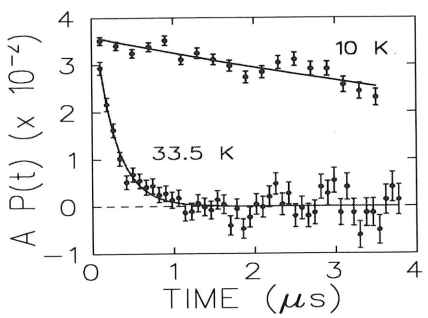

Figure 11. *$Mu@C_{60}$ fast relaxing signal in longitudinal field (redrawn from the original data)*

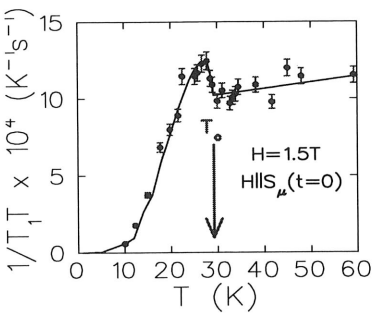

Figure 12. *$Mu@C_{60}$ $(T_1T)^{-1}$ in Rb_3C_{60}, showing a clear Hebel-Slichter peak*

3.3 μSR and Hebel-Slichter peak in novel superconductors

As was pointed out before, Korringa relaxation in metals is too weak to be detected by bare muons, and the more so for the corresponding relaxation in the superconducting state. There is however one notable exception: endohedral muonium in fulleride superconductors.

Muonium does not form in metals. If it did it could not be detected by μSR because it would have an exceedingly short electron T_1, *i.e.* its bound electron would undergo very frequent spin flips, because of the coupling to band electrons. In all C_{60} based materials a fraction of all muons binds to an end of track electron during slowing down and ends up as muonium inside the C_{60} cage. That is *endohedral* muonium ($Mu@C_{60}$), which has a typical yield of around 15 %.

If the fulleride is a metal $Mu@C_{60}$ may be an ideal passive spectator of its electronic properties: it has the very large sensitivity of a paramagnetic center, compared to bare muons, but it is sufficiently removed from the band to have a relatively long electron T_1. The A_3C_{60} salts, where A is an alkali metal, are very interesting superconductors, with critical temperatures exceeding those of traditional BCS materials. It is still an open question whether they can be reconciled with BCS theory or they belong to the family of exotic superconductors, which includes the high T_c cuprates.

In their work on Rb_3C_{60} Kiefl *et al.* (1993) exploited $Mu@C_{60}$ to determine the existence of a Hebel-Slichter peak in the muonium relaxation below $T_c = 29.2K$. The isotropic muonium state is characterised in zero and longitudinal field measurements by a strong temperature dependent relaxation (Figure 11), which corresponds to the Korringa mechanism above T_c. The identification is validated by the magnetic field dependence of the rate.

Figure 12 shows the experimental rate divided by temperature. Above T_c the small slope indicates a deviation from Korringa which is attributed to lattice expansion, while the curve below T_c follows the BCS behaviour.

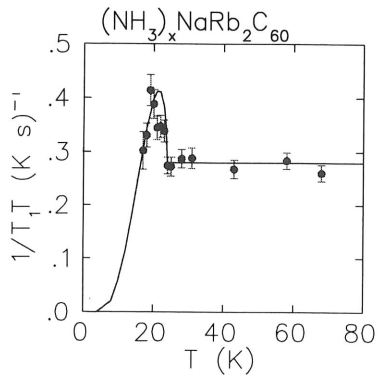

Figure 13. *Hebel-Slichter peak in the T_1^{-1} relaxation rate of NH_3 intercalated in $NaRb_2C_{60}$; the curve is a fit to the Hebel Slichter model*

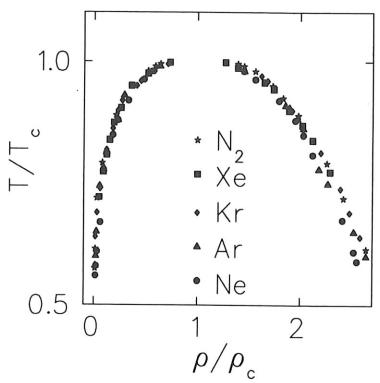

Figure 14. *Guggenheim plot of temperature as a function of density for a series of elements in the gas phase. Both quantities are rescaled for their respective critical values in each individual gas.*

3.4 NMR and Hebel-Slichter peak in novel superconductors

NMR is performed on the same material both on ^{13}C and on alkali metal nuclei. Neither of them shows such clear evidence of the Hebel-Slichter peak as $Mu@C_{60}$. Whereas alkali metal nuclei are spin $I > 1/2$ and the quadrupolar interaction complicates greatly the picture, ^{13}C is a spin $I = 1/2$ like the muon and its different behaviour is more puzzling. An explanation will be offered later on. In this section we concentrate on another $I = 1/2$ NMR nucleus, ^1H, in a slightly different compound: ammonia intercalated $NaRb_2C_{60}$.

The NH_3 molecule shares an interstitial octahedral site with Na. It acts as a neutral lattice spacer, modifying the lattice parameters and the superconducting transition temperatures. This is the original motivation for the study of such compounds: they provide an alternative way to control the structural influence on the electronic properties, besides externally applied pressure and the variation of cation composition. Ammonia also provides an ideal NMR probe: its protons.

Two main results emerge from the proton T_1^{-1} relaxation (Riccò *et al.* 1998): (a) A clear Hebel-Slichter peak is observed; (b) the Korringa relation (Equation 16) does not hold. The first conclusion is self evident from Figure 13. The only open question is why no such peak is observed in the ^{13}C NMR data. We postpone the discussion of this issue.

The Korringa relations require the Knight shift to be measured as well. For ammonia this is not a trivial task and the following considerations apply.

1. At room temperature the ammonia molecules rotate freely inside the interstitial site.

2. The isotropic proton Knight shift is negligible. However a sizeable anisotropic Knight shift is measured. It originates from the pseudodipolar hyperfine interaction (rather then the Fermi contact one), for which the Korringa relations may

be recalculated to yield

$$(\Delta K)^2 T_1 T = \frac{9\hbar}{8\pi k_B}. \tag{18}$$

3. The ammonia protons at low temperature, where molecular rotation is highly restricted, yield the typical powder spectrum of three protons coupled by dipolar interaction; detailed analysis of this spectrum reveals that the molecule is undergoing fast rotation around an axis and that the axis reorientation is restricted (wobbling within a cone). Therefore all measured interaction are effectively reduced by the fast average over the motion. The reduction factor may be derived from the spectrum and applied to the Knight shift (not to the relaxation, which deals with the instantaneous local field).

All this taken into account, the Korringa relation is *not* fulfilled: the Korringa relaxation rate is *weaker* than predicted from the Knight shift. This is normally taken as an indication of the relevance of electron *correlation*. A simple argument follows from the effect of correlation on the electron susceptibility, which is discussed in the lectures of Rainford (1999); in mean field approximation:

$$\chi(q) = \frac{\chi_0(q)}{1 - U\chi_0(q)}$$

where χ_0 is the uncorrelated electron susceptibility (a smooth function of q, with a maximum at $q = 0$) and U is the correlation. Hence the correction introduced by correlation is largest where χ_0 is largest, *i.e.* at $q = 0$. Since the shift $K \propto \chi(0)$ is sensitive to the $q = 0$ component only, while the relaxation $T_1^{-1} \propto \sum_q \chi''(q)/\omega_L$ samples fluctuations of any wave vector q, the former is enhanced more than the latter.

We must however come back to the other NMR results: namely the absence of a Hebel-Slichter peak and the large deviation from the Korringa relation for ^{13}C. The deviation is opposite to that of protons: relaxation rates on carbon are *stronger* than predicted by Korringa. Both effects may be understood by assuming an additional, independent source of relaxation on carbon, say from incipient antiferromagnetic (AF) fluctuations. This particular explanation is supported by the observation of long range antiferromagnetic order at low temperature in the similar compound $NH_3K_3C_{60}$. AF fluctuations grant a larger relaxation rate and the suppression of the Hebel-Slichter peak, which is not present in the magnetic contribution.

The fact that muons and protons do not see AF fluctuations is in itself a very important piece of evidence, which may depends on the detail of a rather complex electronic structure. This may be the bottom line of this example: magnetic resonance experiments on distinct local probes provide complementary information. Their perfect agreement is a check of standard theories, but their partial disagreement may be the much more exciting signature of new phenomena.

At the end of Section 5 we shall see an independent argument by which the ammonia protons should not experience AF fluctuations.

4 Local magnetic probes in critical phenomena

We shall recall a few key concepts on the topic critical phenomena, before describing some classical NMR and μSR experiment related to this subject. Second order thermodynamic transitions take place at a critical point in a phase diagram. Universal behaviours are found in approaching the critical points: for entire families of materials, scaled thermodinamic quantities $a = A(T)/A(0)$ fall on the same curve when plotted as a function of scaled state variables, like for instance the reduced temperature $\epsilon = |(T - T_c)/T_c|$ The original and most famous example of this kind is the plot of Guggenheim (1945), redrawn in Figure 14. The points in this plot represent the value of temperature and pressure which describe the liquid-vapour coexistence curve for each element: when rescaled by the element dependent critical values T_c and ρ_c they all fall on the same curve.

Furthermore, in an interval around the critical point, universal curves like this one are actually expressed by *power* laws, as $a(\epsilon) \propto \epsilon^e$ for $\epsilon \to 0$, where e is a *critical exponent.* The universality of these behaviours resides not only in the fact that many different substances (*e.g.* different gases) share the same critical exponents, but also in that they are shared by distinct phenomena (*e.g.* liquid-vapour and magnetic transitions) for sets of corresponding quantities. For instance the liquid-vapour degree of coexistence curve, $\rho/\rho_c \propto \epsilon^\beta$ and the spontaneous magnetisation of a ferromagnet, $M_s(T)/M_s(0 \propto \epsilon^\beta$, for wide categories of material share the same value of β. Critical exponents are not all independent of one another: thermodynamic relations translate into inequalities and equations linking a number of them. For example the thermodynamic identity $c_H - c_M = T/\chi_T(\frac{\partial M}{\partial T})^2_H$ gives $\alpha+2\beta+\gamma' = 2$ and the analysis of the dependence of $\mathcal{S}(q)$ upon q and ξ gives $\gamma = (2-\eta)\nu$. Table 1 recalls the standard symbol used for a few of these. The first five refer to standard response functions of the liquid-vapour (PVT) and of the ferromagnetic (FM) systems, while the last three refer to the wave vector, space and frequency dependence of the scattering cross section, which may be measured, for instance by neutrons or light.

Symbol	Quantity	System	Expression
δ	degreee of critical isotherm	PVT	$(P - P_c)/P_c \propto ((V - V_c)/V_c)^\delta$
β	degree of the coexistence curve	PVT	$\overline{V_g} - \overline{V_l} \propto \epsilon^\beta$
β	Spontaneous magnetisation	FM	$M(T)/M(0) \propto \epsilon^\beta$
γ	Susceptibility	FM	$\chi_T \propto \epsilon^\gamma$
α	Specific heat	PVT	$c_H, c_M, c_V \propto \epsilon^\alpha$
η	Scattering cross section	all	$\mathcal{S}(H = 0, \epsilon = 0, q) \propto q^{-2+\eta}$
ν	Correlation length	all	$\xi(H = 0, \epsilon) \propto \epsilon^{-\nu}$
z	Width of $S(q, \omega)$)	all	$\Gamma(H = 0, \epsilon, q = 0) = \epsilon^z$

Table 1. *A selection of static and dynamic critical exponents*

The last, z, is a *dynamic* critical exponent: it has to do with the correlation time of critical fluctuations. Notice that its theoretical evaluation requires going beyond standard mean field theory, which does not contain fluctuations at all. This is what makes z so interesting: we know that a mean field model is a good qualitative starting point, but it scores very poorly at quantitative predictions in critical phenomena, the reason being exactly the neglect of fluctuations, which are ever so important at the critical point. And z is *the* parameter most directly connected with fluctuations, as it describes their coherence

in time.

It is clear from the definition of z that, conceptually, the most direct way to measure it is by scattering experiments. However it proved to be quite elusive to a precise determination. We shall now illustrate how local magnetic probes like muons and nuclei give access to dynamic critical exponents. The critical divergence of the relaxation rates is treated in Section 5, but we must anticipate a few fundamental static aspects in the next section.

4.1 Static aspects

The pioneering work in this field was done in the sixties by Jaccarino and Heller, and numerous other authors contributed to a flourishing of more detailed experimental applications in the subsequent decade. In all of them quantitative analysis requires the use of single crystal samples. In relating the NMR aspects I refer mostly to the very nice didactical exposition of Heller (1973) (an "Enrico Fermi" school, perhaps not so easy to find), which in turns summarises earlier papers (Heller and Benedeck1962, Heller 1966).

The first systems to look at are the simple antiferromagnets, *i.e.* the textbook cases of transition metal difluorides. Let us consider for example MnF_2 a tetragonal perovskite structure with $T_N = 67.336$. Its magnetic properties are reported in most solid state textbooks, including Kittel (1966). The ^{19}F nucleus is an ideal $I = 1/2$ NMR probe ($^{19}\gamma/2\pi = 40.07$ MHz/T). It turns out that its coupling to the Mn electron is dominantly hyperfine and isotropic (Shulman and Jaccarino 1957), *i.e.* originated by Fermi contact interaction

$$\gamma\hbar\mathbf{B}_{\rm hf}(T)\cdot\mathbf{I} = \hbar A_{\rm hf}\mathbf{S}(T)\cdot\mathbf{I}. \tag{19}$$

There is also a small dipolar contribution which we shall neglect for simplicity when dealing with NMR relaxation, although it cannot be neglected in connection with shifts.

Figure 15 shows that each fluorine is coupled to three Mn spins. For the sake of simplicity we shall consider that, since each fluorine sees two parallel and one antiparallel Mn spins, a pair of opposite couplings cancel and each F nucleus is effectively coupled to a single Mn spin. We therefore use the same labels, α and β, for the Mn sublattices as for the F ions.

In zero external field and at low temperatures, a single nuclear transition is detected at $\nu_0 = 159.978$ MHz, corresponding to a local field of about 4T. We know by Equation 19 the local field $\mathbf{B}$ to be parallel to $\mathbf{S}$, which in turns lies along the c-axis.

The α and β F sites in the lattice may be distinguished by the application of an external field in a generic direction. As a matter of fact the external field produces a shift, similar to that treated in Schenk (1999). Since the paramagnetic local susceptibility at each Mn ion produces a small local moment, there is always a dipolar contribution at each nucleus. This is different for α and β F sites, for a generic external field direction. Since furthermore domains are present in the ordered phase, which exchange the orientation of α and β sublattices, one sees four distinct NMR resonances (Figure 16, bottom).

In principle there is another distinction between the shift for α and β sites, namely the local susceptibility tensor χ_α, χ_β of the magnetic ion in each sublattice. Since each tensor is obtained obtained by a $\pi/2$ rotation around the c-axis from the other (see Figure 16, top), even neglecting the small dipolar fields one would have four distinct resonances,

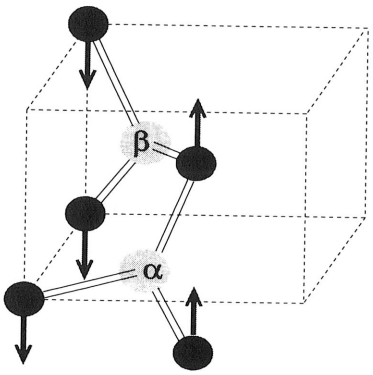

Figure 15. *The perovskite MnF_2: lattice and its magnetic structure*

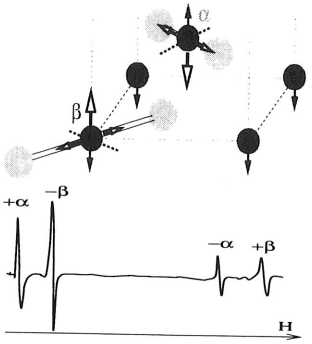

Figure 16. *Top: Orientation of the local susceptibility tensor; Bottom: The four NMR resonances observed below T_N as a function of the applied field intensity.*

corresponding to

$$B_F(\alpha,\beta) = \pm\epsilon B_{\rm hf}\hat{\mathbf{c}} + \mu_0(1 + A_{\rm hf}\underline{\boldsymbol{\chi}}_{\alpha,\beta})\cdot\mathbf{H} \quad (\epsilon = \pm 1).$$

This does not apply to MnF_2, because the Mn χ tensor is isotropic in the a–a' plane, but it does happen in CoF_2, where it was directly detected by muons (De Renzi *et al.* 1984). The dominant interaction for muons is dipolar

$$\gamma\hbar\mathbf{B}^{\rm D}\cdot\mathbf{I}_\alpha = \sum_{i=1}^{2}\mathbf{S}_i\cdot\underline{\mathbf{D}}_{i,\alpha}\cdot\mathbf{I}_\alpha \tag{20}$$

where $\underline{\mathbf{D}}_{i,\alpha}$ is the dipolar tensor due to sublattice α at the muon site i. In the paramagnetic phase the determination of the shift for different orientations of the external field in the lattice frame (see the chapter by Schenk) affords a precise muon site determination. Even if muons stop in just one crystallographically distinct site (the octahedral site, O, of Figure 17) the application of a field makes a number of them inequivalent.

In the paramagnetic region the local moment is $\delta\mathbf{S}_{\alpha,\beta} = \underline{\boldsymbol{\chi}}_{\alpha,\beta}\cdot\mathbf{H}$. The tensor $\underline{\boldsymbol{\chi}}_{\alpha,\beta}$ of the two sublattices is known experimentally and one can predict the angular variation of the precession frequencies from Equation 20. The fit of Figure 18 is unique to site O. Note that this is an important issue for μSR: we have thus identified the stopping site, which is unknown *a priori*, but it is essential for determining exactly the coupling $\underline{\mathbf{D}}$.

In the ordered phase an external field gives rise to even more lines, as shown for instance in the Fourier spectrum of Figure 19, one for each different value of the modulus of the local field

$$B_{\mu,i} = \pm\left(\underline{\mathbf{D}}_{\alpha,i} - \underline{\mathbf{D}}_{\beta,i}\right)\cdot\mathbf{S}(T) + \mu_0\left(1 + (\underline{\mathbf{D}}_{\alpha,i}\cdot\underline{\boldsymbol{\chi}}_\alpha + \underline{\mathbf{D}}_{\beta,i}\cdot\underline{\boldsymbol{\chi}}_\beta\right)\cdot\mathbf{H}. \tag{21}$$

Here too i spans the four inequivalent muon sites and α,β identify the sublattices; the presence of AF domains grants that the dipolar field direction is independent of the

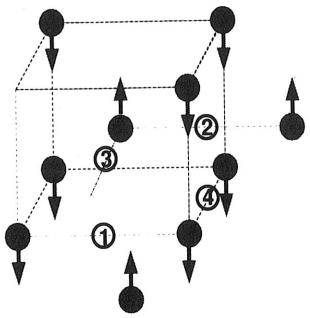

Figure 17. *Magnetically inequivalent O muon sites.*

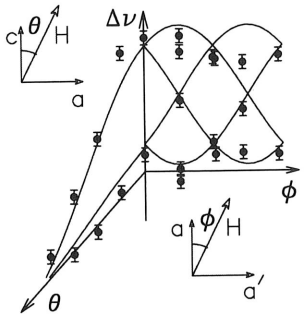

Figure 18. *Precession frequencies in the paramagnetic phase, together with the fit for the O site.*

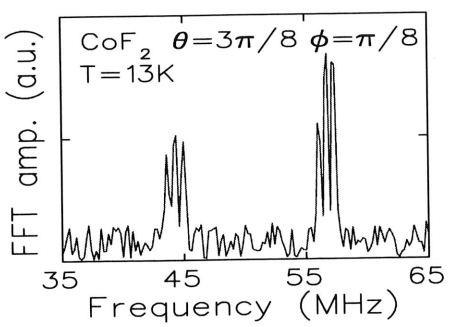

Figure 19. *Fourier spectrum in the ordered phase, (external field of 0.3T).*

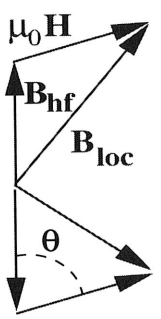

Figure 20. *Vector composition of dipolar and external fields (the shift is neglected here)*

muon site i, hence the $\pm$ sign. For a given field orientation there are twice as many frequencies below than above T_N. The reason lies in the vector composition between the two largest contributions to the local field: the external field and the spontaneous dipolar field, depicted in Figure 20.

Zero field experiments are required in order to measure the magnetic order parameter, *i.e.* the staggered magnetisation $M_S(T) \propto \nu_\mu(T, H = 0)$,[19] $\nu(T, H = 0)$. Figure 21 is redrawn from the NMR data on MnF_2 of Heller (1976), while the Figure 22 is from muons (De Renzi *et al.* 1984a) in CoF_2. Both figures plot the cube of the Larmor frequency in the vicinity of T_N, to show that the critical exponent is $\beta = 1/3$, which agrees within errors with the Ising 3D prediction. Remember that the well known mean field value, from Weiss model, is 0.5.

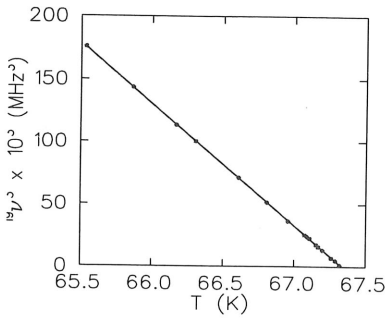

Figure 21. *Cube of the ^{19}F zero field Larmor frequency as a function of temperature in MnF_2*

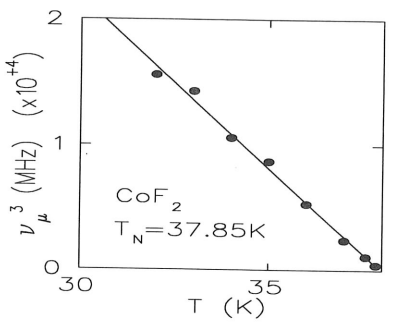

Figure 22. *Cube of the muon zero field Larmor frequency as a function of temperature in CoF_2*

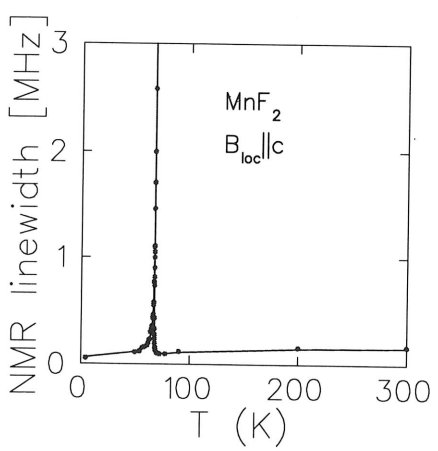

Figure 23. *Critical divergence of the ^{19}F NMR line width in MnF_2*

5 Critical relaxation

Let us consider first the critical divergence of the relaxation rate in TF μSR and in NMR *above* T_N. Figure 23 shows the dramatic effect of critical fluctuations on the line width (*i.e.* on T_2^{-1}) in the original ^{19}F NMR experiment. In a nutshell, approaching T_N fluctuating local fields grow in intensity as their coherence length increases but their correlation time τ becomes longer and longer. Since paramagnetic fluctuations are extremely fast (extreme narrowing regime) their slowing down brings us closer to the resonant relaxation condition, $\tau^{-1} = \omega_L$ – never reaching it, though! .

The detailed analysis for the NMR case with a single isotropic hyperfine coupling is due to Moriya (1962) and it follows from Equation 12. Let us start from the linewidth in a both NMR and TF μSR:

$$\left(\frac{1}{T_2}\right)_z = \frac{\gamma^2}{2}\int_0^\infty dt\Big[\langle h_z(t)h_z(0)\rangle + \frac{1}{2}\left(\langle h_x(t)h_x(0)\rangle + \langle h_y(t)h_y(0)\rangle\right)\Big] \qquad (22)$$

where h_α ($\alpha = x, y, z$ are the components of the fluctuating contribution to the local field and we have chosen $\hat{\mathbf{z}}$ along the static field $\mathbf{B}$. Consider the muon case, where the local fluctuating field is dipolar

$$h_\alpha(t) = \hbar\gamma_e \sum_{i=1}^{N} \frac{3(\mathbf{S}_i(t)\cdot\mathbf{r}_i)r_i^\alpha - r_i^2 S_i^\alpha(t)}{r_i^5} = \sum_{i,\beta} D_{\alpha,\beta}(\mathbf{r}_i) S_i^\beta(t). \tag{23}$$

Notice that the same calculation may be performed in the ordered phase, provided $\mathbf{S}$ is replaced by its fluctuating part $\delta\mathbf{S} = \mathbf{S} - \langle\mathbf{S}\rangle$.

First of all we recognise that the principal axes of $\underline{\mathbf{D}}$ lie along the crystalline directions $\{\hat{\mathbf{a}}, \hat{\mathbf{a}}', \hat{\mathbf{c}}\}$. This is a lucky case since we can write, *e.g.* for $\mathbf{H} \parallel \hat{\mathbf{c}}$

$$\begin{aligned}\left(\frac{1}{T_2}\right)_c = \frac{\gamma^2}{2}\sum_{i,j}[&D_{cc}(\mathbf{r}_i)D_{cc}(\mathbf{r}_j)\int_0^\infty dt\langle S_i^c(t)S_j^c(0)\rangle \\ &+\frac{1}{2}D_{aa}(\mathbf{r}_i)D_{aa}(\mathbf{r}_j)\int_0^\infty dt\langle S_i^a(t)S_j^a(0)\rangle \\ &+\frac{1}{2}D_{a'a'}(\mathbf{r}_i)D_{a'a'}(\mathbf{r}_j)\int_0^\infty dt\langle S_i^{a'}(t)S_j^{a'}(0)\rangle].\end{aligned} \tag{24}$$

This expression is simplified greatly if we use the Fourier expansions

$$S_i^\alpha(t) = \frac{1}{\sqrt{N}}\sum_{\mathbf{q}} S_\alpha(t,\mathbf{q})\exp[i\mathbf{q}\cdot\mathbf{r}_i] \tag{25}$$

$$\langle S_i^\alpha(t)S_j^\alpha(0)\rangle = \frac{1}{N}\sum_{\omega,\mathbf{q}} \mathcal{S}^\alpha(\mathbf{q},\omega)\exp[i\mathbf{q}\cdot(\mathbf{r}_i-\mathbf{r}_j) - i\omega t] \tag{26}$$

$$D_{\alpha,\alpha}(\mathbf{r}_j) = \frac{1}{\sqrt{N}}\sum_{\mathbf{q}} \mathcal{D}_\alpha(\mathbf{q})\exp[i\mathbf{q}\cdot\mathbf{r}_j], \tag{27}$$

for the spin fluctuations, their correlation functions and the dipolar tensor, respectively. Note that the space and time Fourier transform of the electron spin correlation is the scattering function $\mathcal{S}^\alpha(\mathbf{q},\omega)$ (just the diffuse contribution of fluctuations, subtracted of the Bragg peaks). Substituting these quantities into Equation 24 we obtain

$$\left(\frac{1}{T_2}\right)_c = \frac{1}{N}\sum_{\mathbf{q}}\left[|\mathcal{D}_c(\mathbf{q})|^2\,\mathcal{S}^c(\mathbf{q},0) + \frac{1}{2}\left(|\mathcal{D}_a(\mathbf{q})|^2\,\mathcal{S}^a(\mathbf{q},0) + |\mathcal{D}'_a(\mathbf{q})|^2\,\mathcal{S}^{a'}(\mathbf{q},0)\right)\right] \tag{28}$$

where the $\omega = 0$, $\mathbf{q}$-dependent response function appears. Remind that the spin aligns along the c-axis in the ordered phase, and that the order is characterised by an AF wave vector $\mathbf{Q}$. Hence the diverging component of the scattering function is $\mathcal{S}^c(\mathbf{Q})$. A careful data analysis require the non diverging component to be subtracted, *e.g.* by measuring also

$$\left(\frac{1}{T_2}\right)_a \propto \frac{3}{2}\sum_{\mathbf{q}}|\mathcal{D}_a(\mathbf{q})|^2\,\mathcal{S}^a(\mathbf{q},0) + \frac{1}{2}\sum_{\mathbf{q}}|\mathcal{D}_c(\mathbf{q})|^2\,\mathcal{S}^c(\mathbf{q},0). \tag{29}$$

In the following we neglect the non diverging component for the sake of simplicity. Since $\mathcal{D}(\mathbf{q})$ is a smooth function we can approximate Equation 28 as

$$(T_2^{-1})_c \propto |\mathcal{D}_c(\mathbf{Q})|^2\,\mathcal{S}^c(\mathbf{Q},0). \tag{30}$$

It is essentially the same result which is obtained in the NMR case. Our task is to analyze this quantity to determine its critical behaviour. It is worthwhile to stress what Equation 30 tells us in general for nearly critical magnetic fluctuations: nuclei and muons probe these fluctuations through a *structure factor*, $\mathcal{D}_c(\mathbf{Q})$ in this example, which might be zero by symmetry. It is the case, for instance, of a localised probe, symmetrical between two AF sublattices: such a probe does not experience critical relaxation even if the fluctuations go critical!. This structure factor also justifies the difference between ^{13}C and ^{1}H relaxations in fullerides (see Section 3.4). Carbon is sensitive to the on-site spin excitations, whichever their wave vector, while protons, located close to a symmetric octahedral site, are blind to antiferromagnetically correlated fluctuations.

We are describing critical fluctuations by the scattering function of the spin system and it is reasonable to assume that all the relevant features are contained in a single peak around wave vector $\mathbf{Q}$. We can further factorise the contributions to the diverging line width by recalling that the width of $\mathcal{S}(\mathbf{q},\omega)$ is defined as $\Gamma(\mathbf{q})$ and that by fluctuation dissipation theorem the area $\int d\omega \mathcal{S}(\mathbf{q},\omega)$ is proportional to the static $\chi(\mathbf{q})$. We have

$$\mathcal{S}(\mathbf{q},0) \approx \frac{\chi(\mathbf{q})}{\Gamma(\mathbf{q})}.$$

A check of Table 1 reveals that, calling n the line width critical exponent ($T_2^{-1} \simeq \epsilon^{-n}$)

$$n = \nu(z-3) + \gamma \tag{31}$$

since $\sum_{\mathbf{q}} \simeq \kappa^3$, $\Gamma(\mathbf{Q}) \simeq \kappa^z$, $\kappa \simeq \epsilon^{\nu}$, and $\chi(\mathbf{Q}) \simeq \epsilon^{-\gamma}$. This is how the dynamical critical exponent z may be extracted from NMR or μSR data. Theoretical predictions yield $n = 0.35$ for the Heisenberg model and $n = 2/3$ for the Ising model.

Before checking this discussion on the experimental data, let us calculate the asymptotic behaviour of the line width ratio for experiments with $\mathbf{H} \parallel \hat{\mathbf{a}}$ and $\hat{\mathbf{c}}$ respectively. From Equation 29 and the corresponding simplification of Equation 28 we get

$$\frac{\delta\nu_a}{\delta\nu_c} = \frac{1}{2} \qquad (T \to T_N)$$

while far from T_N the fluctuations are isotropic and one computes

$$\frac{\delta\nu_a}{\delta\nu_c} = 1.4 \qquad (T \to \infty)$$

from the dipolar sums. Notice that the two values imply a cross-over.

Figure 24 shows the muon data on MnF_2. The critical power law behaviour as a function of reduced temperature is evident from the log-log plot of the inset. The data do show the expected crossover and a good agreement with the line width anisotropy predictions. The critical exponent is compatible with the Ising model, despite the fact that Mn spin interaction are highly isotropic. This is not really surprising since the spin orders along the c-axis, which means that close enough to T_N the transition is driven by the small residual anisotropy.

The very accurate NMR data of Gottlieb and Heller (1971) on FeF_2, shown in Figure 25 find a value of the dynamical critical exponent even closer to the Ising predictions. Zero field experiments (Hartmann *et al.* 1990, Brown *et al.* 1996), which measure something closer to a T_1^{-1} relaxation, may also be analyzed following the lines described above.

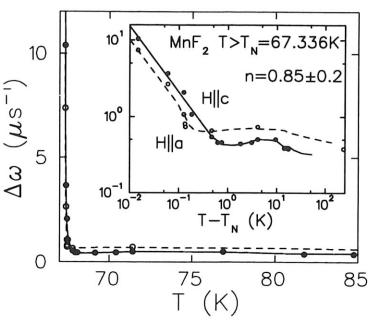

Figure 24. *Muon line width in MnF_2 vs. temperature above T_N; the inset is a log-log plot of the same data, for two orientations*

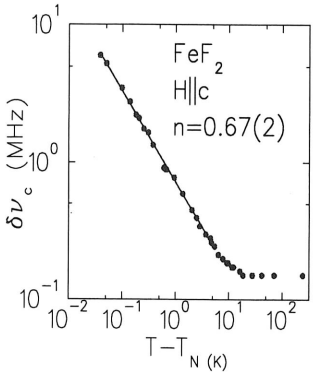

Figure 25. *Log-log plot of the ^{19}F NMR line width in FeF_2 vs. $T - T_N$, showing the power law behaviour and the critical exponent*

Acknowledgments

I wish to thank my colleagues for their many suggestions and precious criticism: Giuseppe Allodi, Cesare Bucci, Sandro Fanesi, Germano Guidi and Mauro Riccò. All residual mistakes are my fault.

Appendix: Relaxation by hyperfine coupling

Let us consider an isotropic medium and use Equation 9 to compute

$$\frac{1}{T_{1,2}} = -\frac{1}{\langle I_{z,+}\rangle}\frac{d\overline{\langle I_{z,+}\rangle}}{dt}.$$

We have to chose a basis set in which to perform the calculation and, since the spin Hamiltonian is

$$\begin{aligned}\mathcal{H}_0 &= \hbar\gamma\mathbf{I}\cdot\mathbf{B} = \hbar\omega I_z \\ \mathcal{H}_1 &= \hbar\omega_0\mathbf{I}\cdot\mathbf{S} = \sum_{l=-1}^{1} F_l A_l\end{aligned}$$

the natural choice is the set of eigenstates of I_z: $I_s\,|m\rangle = m\,|m\rangle$ $(m = \pm 1/2)$. Therefore it is convenient to write:

$$\mathbf{I}\cdot\mathbf{S} = I_z S_z + \frac{1}{2}(I_+ S_- + I_- S_+)$$

and to decompose the interaction (see Equation 5) as follows

$$A_0 = I_z \qquad F_0 = \hbar\omega_0 S_z$$

$$A_{-1} = I_- \qquad F_{-1} = \frac{\hbar\omega_0}{2} S_+$$
$$A_1 = I_+ \qquad F_1 = \frac{\hbar\omega_0}{2} S_-. \tag{32}$$

We can neglect non diagonal components of the tensorial correlation function

$$\overline{F_l(0) F_l'^*(\tau)} = \delta'_{l,l} J_l(\tau). \tag{33}$$

This follows from a two step argument. First of all in a random process $S_\alpha(0)$ and $S_\beta(0)$ are uncorrelated for $\alpha \neq \beta$. Hence at $t = 0$

$$\overline{F_l(0) F_l'^*(0)} = 0.$$

Furthermore if $\omega_L \ll 1/\tau$ then all $J(t)$ decay in a very short time τ and correlation function components for which $\overline{F_l(0) F_l^*(0)} = 1$ are the only ones to survive.

Plugging in 32 and 33, the full expression for T_1^{-1} reads:

$$\frac{1}{T_1} = \frac{1}{\hbar^2 \langle I_z \rangle} \mathrm{Tr} \int_0^\infty d\tau \sum_l \overline{F_l(0) F_{-l}(\tau)} \left[A_l, \left[A^I_{-l}(\tau), \sigma \right] \right] I_z$$

. To proceed one must calculate $A_l^I(\tau) = \exp[i\mathcal{H}_0\tau/\hbar] A_l \exp[-i\mathcal{H}_0\tau/\hbar]$. Calculating the trace with the $|m\rangle$ set one finds that:

$$\langle m| I_z^I |m\rangle' = m\delta'_{m,m} \qquad \langle m| I_+^I |m\rangle' = \delta'_{m-1,m} e^{i\omega t}.$$

For the properties of the trace

$$\frac{1}{T_1} = \frac{1}{\hbar^2 \langle I_z \rangle} Tr \int_0^\infty d\tau \sum_l J_l(\tau) e^{il\omega\tau} \left[A_l, [A_{-l}, I_z] \right] \sigma.$$

By computing the double commutators we get :

$$\frac{1}{T_1} = \frac{2}{\hbar^2} \left(J_{+,-}(\omega) + \text{c.c.} \right)$$

where

$$\begin{aligned} J_{+,-}(\omega) &= \frac{\hbar^2\omega_0^2}{4} \int_0^\infty d\tau \overline{S_-(0) S_+(\tau)} e^{i\omega\tau} \\ &= \frac{\hbar^2\gamma^2}{4} \int_0^\infty d\tau \overline{B_{e,-}(0) B_{e,+}(\tau)} e^{i\omega\tau}. \end{aligned}$$

In an analogous way one finds:

$$\frac{1}{T_2} = \frac{1}{\hbar^2} \left(2J_{+,-}(\omega) + J_{z,z}(0) \right).$$

References

Abragam A, 1961 *The principles of Nuclear Magnetic Resonance* (Oxford Univ. Press, Oxford)

Abragam A, and Goldman M, 1982, *Nuclear magnetism: order and disorder.* (Clarendon Press, Oxford)

Andrew E R, and Tunstall D P, 1961, *Proceeding of the Physical Society* **78,** 1

Brown, S R *et al.* , 1996, Philosophical Magazine Letters **73**, 195

De Renzi, R, et al. (1984) Physical Review B **30** 186

De Renzi, R, et al. (1984a) Physical Review B **30** 197

Ernst R E *et al.* 1987 *Principles of Nuclear Magnetic Resonance in One and Two Dimensions* (Clarendon Press, Oxford)

Fukushima E, and Röder S B W, 1981, *Experimental pulse NMR - A nuts and bolts approach* (Addison-Wesley, Reading, MASS)

Gottlieb, A, and Heller, P (1971), Physical Review B **3**, 3615

Guggenheim Guggenheim E A, 1945, Journal of Chemical Physics, **13**, 253

Kiefl R F *et al.* , 1993, Physical Review Letters **70**, 3987

Hartmann, O *et al.* , 1990, Hyperfine Interactions **64**, 381

Hebel L C, and Slichter C P, 1959, Physical Review **113**, 1504

Heller, P, and Benedeck, G B (1962), Physical Review Letter, **8**, 428

Heller, P (1966), Physical Review, **146**, 403

Heller, P, 1976, *Proprietà locali alle transizioni di fase* (in english), eds. Müller, K A, and Rigamonti, A, p. 447-538 (Società Italiana di Fisica, Bologna)

Kittel, C, 1966, *Introduction to solid state physics*, (J. Wiley, New York) and all more recent editions

Moriya, T, 1962, Progress in Theoretical Physics (Kyoto) **28**, 371

Rainford, B, 1999, contribution to this school

Reif F, 1956, Physical Review **102**, 1417

Riccò, M *et al.* , 1998, Physica C **306**,136

Schenk, A, 1999, contribution to this school

Slichter C P, 1990 *Principles of magnetic resonance*, III Edition (Springer Verlach, Berlin)

Shulman, R G, and Jaccarino, V, 1957, Physical Review **107**, 1196